Finite Element Analysis of an Axisymmetric Elliptic Model with a Localized Gaussian Coefficient

PANYAWAT HAARSA, TEERASAK CHALADGARN
Department of Mathematics, Faculty of Science,
Srinakharinwirot University, Bangkok,
THAILAND

Abstract: - This study investigates a variable-coefficient elliptic problem with a localized Gaussian coefficient. The model is motivated by a steady electroquasistatic problem and adopts an unweighted two-dimensional meridional formulation. The coefficient amplitude and localization parameters are analyzed separately. Uniform coercivity is preserved because the coefficient remains bounded below by one. In contrast, the derived coefficient-gradient bound scales with the product of the amplitude and the square root of the localization parameter. A parameter-explicit regularity estimate is established and incorporated into the finite element error analysis. A conforming approximation is then studied. Theoretical estimates establish first-order convergence in the -seminorm and second-order convergence in the -norm. Numerical experiments confirm these rates. A mesh-localization indicator is introduced to describe spatial resolution relative to the localization length. The conditioning study shows that the estimated 1-norm condition number increases with both amplitude and localization. Finally, incomplete-Cholesky-preconditioned CG substantially reduces the variation in iteration counts compared with unpreconditioned CG over the tested parameter ranges.

Key-Words: - Variable-coefficient elliptic problem, finite element method, localized Gaussian coefficient, stiffness-matrix conditioning, incomplete Cholesky preconditioning, axisymmetric elliptic model, parameter-explicit error estimates, mesh-localization indicator

Received: May 8, 2026. Revised: July 14, 2026. Accepted: August 15, 2026. Published: November 25, 2026.

1 Introduction

Elliptic partial differential equations with spatially varying coefficients arise in many models of heterogeneous media. Localized coefficient variation is particularly important because it can preserve uniform ellipticity while producing strong spatial gradients. Variational formulations and finite element methods provide standard tools for the analysis of such problems [1], [2], [3], [4], [5]. In electromagnetic applications, related Maxwell formulations and finite element studies also emphasize the influence of material heterogeneity on stability and numerical approximation [6], [7], [8], [9], [10].

Coefficient variation also affects the algebraic properties of the discrete problem. Large contrast can deteriorate stiffness-matrix conditioning and increase the cost of iterative solution. These effects motivate the use of efficient sparse solvers and preconditioning techniques [11], [12], [13], [14], [15], [16], [17]. Variable-coefficient elliptic problems on cylindrical domains provide a related numerical setting [18]. However, the separate roles of coefficient amplitude and spatial localization are not always made explicit. In particular, stronger localization may increase spatial variation without reducing the uniform lower ellipticity bound.

The present study considers a two-dimensional meridional elliptic model motivated by a steady electroquasistatic problem. The material coefficient is represented by the localized Gaussian profile

$$a(z) = 1 + A\exp\left[-\alpha(z - z_0)^2\right],$$

where $A \geq 0$ controls the amplitude and $\alpha > 0$ controls the localization. The model uses an unweighted meridional formulation. It therefore retains the principal variable-coefficient elliptic structure while allowing the effects of localized heterogeneity to be studied explicitly. The work does not introduce a new finite element scheme. Instead, it develops a parameter-explicit analysis for a standard conforming P_1 approximation.

The main objective is to separate continuous stability from localization-dependent regularity and discrete conditioning. The uniform bound $a(z) \geq 1$ yields a coercivity constant that is independent of both A and α. In contrast, the derived coefficient-gradient bound scales with $A\sqrt{\alpha}$. This dependence enters the higher-order regularity bound and the finite element error constants. A characteristic localization length is

also introduced to relate coefficient variation to mesh resolution.

The finite element analysis establishes first-order convergence in the $H^1(\Omega)$ -seminorm and second-order convergence in the $L^2(\Omega)$ -norm [1], [3], [4], [5]. The analysis retains explicit dependence on the Gaussian parameters. A refined finite-domain contrast factor is then used to examine stiffness-matrix conditioning. Numerical experiments study convergence, mesh-localization interaction, and parameter-dependent conditioning. The performance of unpreconditioned CG and incomplete-Cholesky-preconditioned CG is also compared [11], [13], [16].

The numerical results confirm the expected finite element convergence orders over the tested localization regimes. They also show that the mesh-localization quantity is better interpreted as a geometric resolution indicator than as a direct predictor of the error magnitude. The estimated matrix condition number increases with both amplitude and localization on a fixed mesh. Incomplete Cholesky preconditioning substantially reduces the variation in CG iteration counts over the parameter ranges considered.

2 Methods

This section introduces the reduced elliptic model, localized Gaussian coefficient, and computational domain.

2.1 Maxwell-based elliptic model

Consider a conducting medium in a steady electroquasistatic regime. We assume that inductive effects are negligible, so that the electric field is irrotational. The electric field $\mathbf{E}$, current density $\mathbf{J}$, and scalar electric potential ϕ satisfy [6], [7]

$$\nabla\times\mathbf{E}=0,\qquad \mathbf{J}=\sigma(z)\mathbf{E},\qquad \nabla\cdot\mathbf{J}=s.$$

where $\sigma(z)>0$ denotes the conductivity and s represents an impressed source. Since $\nabla\times\mathbf{E}=0$, we write $\mathbf{E}=-\nabla\phi$. Substitution into the current-conservation equation gives $-\nabla\cdot\left(\sigma(z)\nabla\phi\right)=s$. For an axisymmetric configuration, the material coefficient is assumed to depend only on the depth coordinate z. After normalization by a positive constant background conductivity $\sigma_b>0$, we define $a(z)=\sigma(z)/\sigma_b$, $f=s/\sigma_b$ and set $u:=\phi$. The resulting dimensionless-coefficient elliptic model studied below is therefore $-\nabla\cdot\left(a(z)\nabla u\right)=f$ in Ω, where u denotes the scalar potential in the two-dimensional meridional model. In the present study, we adopt the corresponding unweighted two-dimensional meridional model. This formulation preserves the principal variable-coefficient elliptic structure associated with the axisymmetric setting while allowing the effects of localized material heterogeneity to be analyzed explicitly.

2.2 Localized Gaussian coefficient

The normalized material coefficient is modeled by

$$a(z)=1+A\exp\left[-\alpha(z-z_0)^2\right],$$

where $A\ge 0$ is the amplitude, $\alpha>0$ is the localization parameter, and $z_0\in(0,Z)$ specifies the center of the localized perturbation. The parameter A controls the perturbation amplitude and contributes directly to the uniform coefficient-contrast bound, whereas increasing α produces a narrower and more strongly localized profile. Since $0<\exp\left[-\alpha(z-z_0)^2\right]\le 1$, the coefficient satisfies $1\le a(z)\le 1+A$. Hence, the coefficient remains strictly positive for all $A\ge 0$ and $\alpha>0$. For the parameter-robust analysis, we use the uniform ellipticity bounds $\underline{a}=1$, $\bar{a}=1+A$, so that $\underline{a}\le a(z)\le\bar{a}$. These are uniform bounding constants and need not coincide with the exact extrema of a on the bounded computational domain. These bounds show that localization does not cause a loss of uniform ellipticity. However, α strongly affects the spatial variation of the coefficient. Indeed, $a'(z)=-2A\alpha(z-z_0)\exp\left[-\alpha(z-z_0)^2\right]$, and therefore

$$\|\nabla a\|_{L^\infty(\Omega)}=\|a'\|_{L^\infty(0,Z)}\le A\sqrt{2\alpha/e}.$$

Thus, although α does not enter the parameter-robust uniform ellipticity-ratio bound $\bar{a}/\underline{a}=1+A$, it strongly influences the spatial variation of the coefficient. For fixed A, the derived upper bound for the coefficient gradient scales as $O(A\sqrt{\alpha})$. This distinction will be used later to explain the different effects of amplitude and localization on regularity, mesh resolution, and discrete conditioning.

2.3 Computational domain and boundary conditions

Let $\Omega=(0,R)\times(0,Z)\subset\mathbb{R}^2$ denote the bounded meridional computational domain with coordinates (r,z), where $R>0$ and $Z>0$. The domain Ω is rectangular and therefore is a bounded Lipschitz and convex polygonal domain. Throughout the theoretical analysis and numerical experiments, we impose the homogeneous Dirichlet boundary condition $u=0$

on $\partial\Omega$. Accordingly, the boundary-value problem considered in the remainder of this study is

$$\begin{cases} -\nabla\cdot\big(a(z)\nabla u\big) = f, & \text{in } \Omega, \\ u = 0, & \text{on } \partial\Omega. \end{cases}$$

For the Gaussian coefficient introduced in Section 2.2, the parameter-robust bounds $1 \le a(z) \le 1+A$ hold throughout Ω. Hence, the problem is uniformly elliptic, with the parameter-independent lower ellipticity bound $a(z) \ge 1$ for all admissible values of A and α. The rectangular geometry and homogeneous Dirichlet condition also provide the setting used in the variational formulation, elliptic regularity analysis, and conforming finite element approximation developed in Sections 3 and 4.

3 Weak formulation and parameter-dependent analysis

We now formulate the boundary-value problem of Section 2 in a variational setting. The analysis establishes the continuity and coercivity of the associated bilinear form, followed by existence and uniqueness of the weak solution. Particular attention is given to the explicit dependence of the analytical estimates on the Gaussian coefficient parameters A and α. The distinction between coefficient contrast and coefficient localization will also be used in the regularity and finite element analyses [2], [5].

We consider $-\nabla\cdot\big(a(z)\nabla u\big) = f$ in Ω, with $u = 0$ on $\partial\Omega$, where

$$a(z) = 1 + A\exp\Big[-\alpha(z - z_0)^2\Big], \qquad A \ge 0, \quad \alpha > 0.$$

As established in Section 2.2, $1 \le a(z) \le 1+A$. Thus, the problem is uniformly elliptic, with the parameter-independent lower bound $a(z) \ge 1$ for all admissible values of A and α. However, the coefficient gradient satisfies $\|\nabla a\|_{L^\infty(\Omega)} \le A\sqrt{2\alpha/e}$. Hence, for fixed A, increasing α increases the derived upper bound on the spatial variation of the coefficient, while the lower ellipticity bound remains unchanged. This distinction is important in the parameter-dependent estimates developed below.

3.1 Functional setting

Let $\Omega \subset \mathbb{R}^2$ be a bounded Lipschitz domain. We introduce the Sobolev space $V = H_0^1(\Omega)$, equipped with the norm $\|v\|_V = \|\nabla v\|_{L^2(\Omega)}$. By Poincaré's inequality, there exists a constant $C_P > 0$, depending only on Ω, such that [2], [5] $\|v\|_{L^2(\Omega)} \le C_P \|\nabla v\|_{L^2(\Omega)}$ for all $v \in V$. Hence, $\|\nabla v\|_{L^2(\Omega)}$ defines a norm on V equivalent to the standard $H^1(\Omega)$ -norm. For $f \in L^2(\Omega)$, define the linear functional

$$\ell(v) = \int_\Omega f v dx, \qquad v \in V.$$

Using the Cauchy–Schwarz and Poincaré inequalities, we obtain

$$|\ell(v)| \le \|f\|_{L^2(\Omega)}\|v\|_{L^2(\Omega)} \le C_P \|f\|_{L^2(\Omega)}\|v\|_V .$$

Therefore, $\ell \in V'$, $\|\ell\|_{V'} \le C_P \|f\|_{L^2(\Omega)}$, where $V' = (H_0^1(\Omega))' = H^{-1}(\Omega)$ denotes the dual space of V. The weak formulation and the parameter-dependent properties of the associated bilinear form are established in the following subsections.

3.2 Weak formulation and bilinear form

Let $V = H_0^1(\Omega)$ be the space introduced in Section 3.1. Multiplying the governing equation $-\nabla\cdot\big(a(z)\nabla u\big) = f$ by an arbitrary test function $v \in V$ and integrating over Ω, we obtain

$$-\int_\Omega \nabla\cdot\big(a(z)\nabla u\big) v dx = \int_\Omega f v dx.$$

Using Green's identity and the vanishing trace of $v \in H_0^1(\Omega)$, we obtain [1], [2], [3], [5]

$$\int_\Omega a(z)\nabla u\cdot\nabla v dx = \int_\Omega f v dx.$$

We therefore define the bilinear form

$$\mathrm{A}(u,v) = \int_\Omega a(z)\nabla u\cdot\nabla v dx, \qquad u, v \in V,$$

and the linear functional $\ell(v) = \int_\Omega f v dx$, $v \in V$. The weak problem is then stated as follows: find $u \in V$ such that $\mathrm{A}(u,v) = \ell(v)$ for all $v \in V$. Since $a(z)$ is real-valued and strictly positive, the bilinear form is symmetric,

$$\mathrm{A}(u,v) = \mathrm{A}(v,u),$$

and $\mathrm{A}(v,v) = \int_\Omega a(z)|\nabla v|^2 dx \ge \|\nabla v\|^2_{L^2(\Omega)} > 0$ for every nonzero $v \in V$. This motivates the coefficient-weighted energy norm $\|v\|_{\mathrm{A}} := \big(\mathrm{A}(v,v)\big)^{1/2}$. Using $1 \le a(z) \le 1+A$, we immediately obtain $\|v\|_V \le \|v\|_{\mathrm{A}} \le \sqrt{1+A}\,\|v\|_V$. Thus, the energy norm is equivalent to the V -norm. The upper norm-equivalence constant depends on the amplitude A, whereas the localization parameter α does not enter the parameter-robust uniform coefficient bounds. The continuity and coercivity consequences of these estimates are established in Section 3.3.

3.3 Continuity and coercivity

The well-posedness of the weak problem depends on the continuity and coercivity of the bilinear form

$\mathrm{A}(\cdot,\cdot)$. For the Gaussian coefficient introduced in Section 2.2, we use the uniform bounds $\underline{a}=1,\ \bar{a}=1+A,$ so that $\underline{a}\le a(z)\le\bar{a}$ for all $(r,z)\in\Omega.$ These bounds are independent of the localization parameter α.

Lemma 3.1. Let
$a(z)=1+A\exp\left[-\alpha(z-z_0)^2\right],\ A\ge 0,\ \alpha>0,\ z_0\in(0,Z)$.
Then the bilinear form

$$\mathrm{A}(u,v)=\int_\Omega a(z)\nabla u\cdot\nabla v dx.$$

is continuous and coercive on $V=H_0^1(\Omega).$ More precisely, $|\mathrm{A}(u,v)|\le(1+A)\|u\|_V\|v\|_V$ for all $u,v\in V,$ and
$\mathrm{A}(v,v)\ge\|v\|_V^2$ for all $v\in V.$ Hence, the continuity and coercivity constants may be chosen as $C_{\mathrm{cont}}=1+A,$ $C_{\mathrm{coer}}=1.$

Proof. Since $a(z)\le 1+A$, the Cauchy–Schwarz inequality gives [2], [3], [5]

$$|\mathrm{A}(u,v)|=\left|\int_\Omega a(z)\nabla u\cdot\nabla v dx\right|\le(1+A)\|\nabla u\|_{L^2(\Omega)}\|\nabla v\|_{L^2(\Omega)}$$
$$=(1+A)\|u\|_V\|v\|_V .$$

Thus, A is continuous with $C_{\mathrm{cont}}=1+A.$ Similarly, since $a(z)\ge 1$, we obtain

$$\mathrm{A}(v,v)=\int_\Omega a(z)|\nabla v|^2\,dx\ge\int_\Omega|\nabla v|^2\,dx=\|v\|_V^2 .$$

Therefore, A is coercive with $C_{\mathrm{coer}}=1.$ This completes the proof.

The above estimates separate the effects of amplitude and localization at the level of uniform ellipticity. The amplitude A enters the continuity constant through the upper coefficient bound $1+A.$ In contrast, neither A nor α reduces the uniform coercivity constant because $a(z)\ge 1.$ The localization parameter α therefore does not enter the uniform coefficient bounds used in the continuity and coercivity estimates. Its influence appears instead through the spatial variation of $a(z)$, quantified by $\|\nabla a\|_{L^\infty(\Omega)}\le A\sqrt{2\alpha/e},$ which will be used in the parameter-dependent regularity analysis.

3.4 Existence, uniqueness, and parameter-robust stability

We now establish the well-posedness of the weak problem. The estimates obtained in Sections 3.1–3.3 allow the stability constant to be stated explicitly.

Theorem 3.2. Let $\Omega\subset\mathbb{R}^2$ be a bounded Lipschitz domain, and let $a(z)=1+A\exp\left[-\alpha(z-z_0)^2\right],$ $A\ge 0,\ \alpha>0,\ z_0\in(0,Z).$ For every $f\in L^2(\Omega),$ there exists a unique weak solution $u\in V=H_0^1(\Omega)$ satisfying $\mathrm{A}(u,v)=\ell(v)$ for all $v\in V.$ Moreover,

$$\|u\|_V\le C_P\|f\|_{L^2(\Omega)},$$

where C_P is the Poincaré constant of $\Omega.$ In particular, this stability bound is independent of both A and α.

Proof. By Lemma 3.1, the bilinear form $\mathrm{A}(\cdot,\cdot)$ is continuous and coercive on V, with $C_{\mathrm{cont}}=1+A,$ $C_{\mathrm{coer}}=1.$ From Section 3.1, $\|\ell\|_{V'}\le C_P\|f\|_{L^2(\Omega)}$. Hence, all assumptions of the Lax–Milgram theorem are satisfied [2], [5]. Therefore, the weak problem admits a unique solution $u\in V.$ Taking $v=u$ in the weak formulation gives $\mathrm{A}(u,u)=\ell(u).$ Using coercivity, $\|u\|_V^2\le\mathrm{A}(u,u),$ while the Cauchy–Schwarz and Poincaré inequalities yield

$$|\ell(u)|\le C_P\|f\|_{L^2(\Omega)}\|u\|_V .$$

Consequently, $\|u\|_V^2\le C_P\|f\|_{L^2(\Omega)}\|u\|_V$. If $u=0$, the estimate is immediate. Otherwise, dividing by $\|u\|_V$ yields $\|u\|_V\le C_P\|f\|_{L^2(\Omega)}$. This completes the proof.

The estimate shows that the $H_0^1(\Omega)$ -stability of the continuous problem is parameter robust. In particular, neither increasing A nor increasing α reduces the uniform coercivity lower bound because $a(z)\ge 1.$ A deterioration of the discrete condition number as α increases should therefore not be interpreted as a loss of continuous coercivity. Instead, for fixed $A,$ stronger localization is reflected in the increasing upper bound on the spatial variation of the coefficient, quantified by $\|\nabla a\|_{L^\infty(\Omega)}\le A\sqrt{2\alpha/e},$ which becomes relevant to higher-order regularity, approximation constants, and mesh resolution.

3.5 Parameter-dependent coefficient estimates

The uniform ellipticity bounds describe the effect of the amplitude parameter A, but they do not capture the spatial localization induced by α. We therefore derive additional coefficient estimates that explicitly separate these two effects.

Proposition 3.3. Let
$a(z)=1+A\exp\left[-\alpha(z-z_0)^2\right],\ A\ge 0,\ \alpha>0,\ z\in(0,Z)$.
Then $1\le a(z)\le 1+A,$ and $\|a-1\|_{L^\infty(\Omega)}\le A.$ Moreover,

$\| \nabla a \|_{L^\infty(\Omega)} \le A\sqrt{2\alpha / e}$.

Proof. The first two estimates follow directly from $0 < \exp\left[-\alpha(z-z_0)^2\right] \le 1$. Since a depends only on z, $\nabla a(r,z) = \left(0, -2A\alpha(z-z_0)\exp\left[-\alpha(z-z_0)^2\right]\right)$. Hence, $|\nabla a(r,z)| = 2A\alpha\,|z-z_0|\exp\left[-\alpha(z-z_0)^2\right]$. Let $t = \sqrt{\alpha}\,|z-z_0|$. Then $|\nabla a(r,z)| = 2A\sqrt{\alpha}te^{-t^2}$. The function te^{-t^2} attains its maximum at $t = 1/\sqrt{2}$, with $\max_{t\ge 0} te^{-t^2} = 1/\sqrt{2e}$. Therefore, $\| \nabla a \|_{L^\infty(\Omega)} \le A\sqrt{2\alpha / e}$. This completes the proof.

The estimates reveal two distinct parameter mechanisms. A parameter-robust upper bound for the coefficient contrast is given by the uniform ellipticity ratio $\bar{a} / \underline{a} = 1 + A$, whereas a convenient gradient-based measure of localization is $G(A,\alpha) := A\sqrt{2\alpha / e}$. Thus, A enters both the uniform contrast bound and the spatial-variation bound, while α enters the spatial-variation bound. The exact finite-domain coefficient contrast, which also depends on α , is quantified separately in Section 4.3. A natural localization length associated with the Gaussian perturbation is $\ell_\alpha = \alpha^{-1/2}$. Indeed, the Gaussian factor decreases to e^{-1} at the characteristic distance $|z - z_0| = \ell_\alpha$. Hence, increasing α decreases the characteristic localization length according to $\ell_\alpha = \alpha^{-1/2}$. The coefficient-gradient estimate may equivalently be written as

$$\| \nabla a \|_{L^\infty(\Omega)} \le \sqrt{\frac{2}{e}} \cdot \frac{A}{\ell\alpha}.$$

For a mesh with characteristic size h , this motivates the dimensionless mesh-localization parameter $\eta_h = h / \ell_\alpha = h\sqrt{\alpha}$. Small values of η_h correspond to a mesh that is fine relative to the localization scale, whereas larger values indicate that the localized coefficient variation is less well resolved. No universal resolution threshold is implied by this definition. The numerical influence of η_h will be examined in Section 5. Finally, since $a \in W^{1,\infty}(\Omega)$, the preceding gradient estimate allows the coefficient dependence of the elliptic regularity constant to be quantified explicitly [2], [5]. This is developed in Section 3.6.

3.6 Parameter-explicit elliptic regularity

The $H_0^1(\Omega)$ -stability estimate in Theorem 3.2 is independent of A and α . Higher-order regularity, however, is sensitive to the spatial variation of the coefficient. We now quantify this dependence. Assume that $\Omega \subset \mathbb{R}^2$ is a bounded convex polygonal domain, as satisfied by the rectangular computational domain introduced in Section 2.3.

Proposition 3.4. Let $\Omega \subset \mathbb{R}^2$ be a bounded convex polygonal domain, let $f \in L^2(\Omega)$, and let $a(z) = 1 + A\exp\left[-\alpha(z-z_0)^2\right]$, $A \ge 0$, $\alpha > 0$, $z \in (0, Z)$. Let $u \in H_0^1(\Omega)$ be the weak solution of $-\nabla \cdot \left(a(z)\nabla u\right) = f$ in Ω . Then $u \in H^2(\Omega) \cap H_0^1(\Omega)$, and there exists a constant $C_{reg} > 0$, depending only on Ω , such that

$$\| u \|_{H^2(\Omega)} \le C_{\text{reg}} \left(1 + C_P A\sqrt{2\alpha / e}\right) \| f \|_{L^2(\Omega)} .$$

Proof. In the sense of distributions, expanding the divergence term gives $-a(z)\Delta u - \nabla a \cdot \nabla u = f$. Since $a(z) \ge 1$, we have $\| 1/a \|_{L^\infty(\Omega)} \le 1$. Therefore, $-\Delta u = \dfrac{f}{a(z)} + \dfrac{\nabla a}{a(z)} \cdot \nabla u$. Hence,

$$\begin{aligned} \| \Delta u \|_{L^2(\Omega)} &\le \| f / a \|_{L^2(\Omega)} + \| (\nabla a / a).\nabla u \|_{L^2(\Omega)} \\ &\le \| f \|_{L^2(\Omega)} + \| \nabla a \|_{L^\infty(\Omega)} \| \nabla u \|_{L^2(\Omega)} . \end{aligned}$$

From Theorem 3.2, $\| \nabla u \|_{L^2(\Omega)} = \| u \|_V \le C_P \| f \|_{L^2(\Omega)}$.

Using Proposition 3.3,

$$\| \nabla a \|_{L^\infty(\Omega)} \le A\sqrt{2\alpha / e},$$

we obtain

$$\| \Delta u \|_{L^2(\Omega)} \le \left(1 + C_P A\sqrt{2\alpha / e}\right) \| f \|_{L^2(\Omega)} .$$

Hence, $\Delta u \in L^2(\Omega)$.

For a bounded convex polygonal domain $\Omega \subset \mathbb{R}^2$ with homogeneous Dirichlet boundary conditions, the standard Poisson H^2 -regularity estimate gives [2], [5] $\| u \|_{H^2(\Omega)} \le C_{\text{reg}} \| \Delta u \|_{L^2(\Omega)}$. Combining the preceding estimates yields

$$\| u \|_{H^2(\Omega)} \le C_{\text{reg}} \left(1 + C_P A\sqrt{2\alpha / e}\right) \| f \|_{L^2(\Omega)} .$$

This completes the proof.

The estimate separates continuous stability from higher-order regularity. Uniform coercivity remains independent of A and α, whereas the explicit H^2 -regularity upper bound contains a parameter-dependent contribution proportional to $A\sqrt{\alpha}$. Equivalently, using the localization length $\ell_\alpha = \alpha^{-1/2}$, this contribution is proportional to A / ℓ_α. Thus, stronger amplitude or sharper localization increases the explicit upper bound obtained for the regularity

constant, even though uniform ellipticity is preserved. This dependence will enter the finite element error estimates and provides a theoretical basis for studying the interaction between localization and mesh resolution.

4 Finite element discretization and parameter-dependent error analysis

We now construct a conforming finite element approximation of the weak problem. The analysis first establishes the discrete formulation and then derives error estimates that retain the explicit dependence on the Gaussian parameters A and α. Particular attention is given to the interaction between mesh resolution and the localization scale introduced in Section 3.5. The conditioning of the resulting stiffness matrix is examined subsequently.

4.1 Finite element space and discrete problem

Let T_h be a conforming, shape-regular triangulation of Ω. For each element $K \in \mathrm{T}_h$, let $h_K = \mathrm{diam}(K)$, and define $h = \max_{K\in\mathrm{T}_h} h_K$. The conforming piecewise-linear finite element space is [1], [3], [5]

$V_h = \{v_h \in C^0(\bar{\Omega}) : v_h|_K \in P_1(K) \text{ for all } K \in \mathrm{T}_h, \ v_h = 0 \text{ on } \partial\Omega\}$. Then $V_h \subset H_0^1(\Omega) = V$. The Galerkin finite element problem is to find $u_h \in V_h$ such that [1], [3], [5]

$$\mathrm{A}(u_h, v_h) = \ell(v_h) \text{ for all } v_h \in V_h,$$

where $\mathrm{A}(u_h, v_h) = \int_\Omega a(z)\nabla u_h \cdot \nabla v_h dx$ and $\ell(v_h) = \int_\Omega f v_h dx$. Since $V_h \subset V$, the continuity and coercivity estimates of Lemma 3.1 remain valid on V_h. In particular, $|\mathrm{A}(w_h, v_h)| \le (1+A)\| w_h \|_V \| v_h \|_V$ and $\mathrm{A}(v_h, v_h) \ge \| v_h \|_V^2$. Therefore, the finite-dimensional Galerkin problem admits a unique solution $u_h \in V_h$. Let $\{\varphi_i\}_{i=1}^{N_h}$ be the nodal basis of V_h, and write $u_h = \sum_{j=1}^{N_h} U_j \varphi_j$. The Galerkin problem is equivalent to the linear system $K_h U = F$, where the stiffness matrix and load vector are defined by $(K_h)_{ij} = \int_\Omega a(z)\nabla\varphi_j \cdot \nabla\varphi_i dx$ and $F_i = \int_\Omega f\varphi_i, dx$. Since $a(z) \ge 1$, the stiffness matrix K_h is symmetric positive definite. Consequently, both direct solvers and conjugate-gradient-type iterative methods can be applied to the discrete system [5], [13]. The localization length $\ell_\alpha = \alpha^{-1/2}$ provides a natural scale for assessing whether the mesh resolves the localized coefficient. On an element K, we therefore introduce the local mesh-localization ratio $\eta_K := (h_K / \ell_\alpha) = h_K\sqrt{\alpha}$. For a uniform mesh, this reduces to $\eta_h = h\sqrt{\alpha}$. These quantities do not alter the Galerkin formulation. They will be used to interpret the parameter-dependent approximation estimates and the numerical mesh-resolution study.

4.2 Parameter-dependent a priori error estimates

Let $u \in V$ and $u_h \in V_h$ denote the exact and finite element solutions, respectively. Subtracting the continuous and discrete variational problems gives the Galerkin orthogonality [1], [3], [5] $\mathrm{A}(u - u_h, v_h) = 0$ for all $v_h \in V_h$. Since $\mathrm{A}(\cdot,\cdot)$ is symmetric and coercive, the Galerkin solution is the best approximation in the energy norm [3], [4], [5]: $\| u - u_h \|_{\mathrm{A}} \le \inf_{v_h\in V_h} \| u - v_h \|_{\mathrm{A}}$.

Under the assumptions of Proposition 3.4, $u \in H^2(\Omega) \cap H_0^1(\Omega)$. Let $I_h u \in V_h$ denote the nodal interpolant of u. For conforming P_1 elements on a shape-regular mesh, $\| \nabla(u - I_h u) \|_{L^2(\Omega)} \le C_I h \| u \|_{H^2(\Omega)}$, where C_I depends only on the shape regularity of the mesh [1], [3], [5]. Since $\| v \|_{\mathrm{A}}^2 \le (1+A)\| \nabla v \|_{L^2(\Omega)}^2$, we obtain

$$\| u - u_h \|_{\mathrm{A}} \le C_I h\sqrt{1+A}\, \| u \|_{H^2(\Omega)}.$$

Because $\| u - u_h \|_V \le \| u - u_h \|_{\mathrm{A}}$, Proposition 3.4 yields the following parameter-explicit estimate.

Theorem 4.1. Under the assumptions of Proposition 3.4, there exists a constant $C > 0$, depending only on the domain and the mesh shape-regularity constant but independent of h, A, and α, such that

$$\| u - u_h \|_V \le Ch\sqrt{1+A}\left(1 + C_P A\sqrt{2\alpha/e}\right) \| f \|_{L^2(\Omega)}.$$

Moreover,

$$\left\| u - u_h \right\|_{L^2(\Omega)} \le Ch^2(1+A)\left(1 + C_P A\sqrt{2\alpha/e}\right)^2 \left\| f \right\|_{L^2(\Omega)}.$$

Proof. By Galerkin orthogonality and the best-approximation property in the energy norm,

$$\left\| u - u_h \right\|_{\mathrm{A}} \le \inf_{v_h\in V_h} \left\| u - v_h \right\|_{\mathrm{A}} \le \left\| u - I_h u \right\|_{\mathrm{A}}.$$

Using $a(z) \le 1 + A$ and the interpolation estimate,

$$\begin{aligned} \left\| u - I_h u \right\|_{\mathrm{A}} &\le \sqrt{1+A} \left\| \nabla\left(u - I_h u\right) \right\|_{L^2(\Omega)} \\ &\le C_I h\sqrt{1+A} \left\| u \right\|_{H^2(\Omega)}. \end{aligned}$$

Since $\left\| u - u_h \right\|_V \le \left\| u - u_h \right\|_{\mathrm{A}}$, Proposition 3.4 gives

$$\left\| u - u_h \right\|_V \le Ch\sqrt{1+A}\left(1 + C_P A\sqrt{2\alpha/e}\right) \left\| f \right\|_{L^2(\Omega)}.$$

This proves the first estimate. An L^2-error estimate follows from the Aubin–Nitsche duality argument [1],

[3], [5]. Let $e_h = u - u_h$, and consider the dual problem: find $\psi \in H_0^1(\Omega)$ such that

$$\mathrm{A}(v,\psi) = (e_h, v)_{L^2(\Omega)} \text{ for all } v \in H_0^1(\Omega).$$

By Proposition 3.4,

$$\| \psi \|_{H^2(\Omega)} \le C_{\mathrm{reg}} \left(1 + C_P A\sqrt{2\alpha / e}\right) \| e_h \|_{L^2(\Omega)} .$$

Using Galerkin orthogonality,

$$\| e_h \|_{L^2(\Omega)}^2 = \mathrm{A}(e_h, \psi) = \mathrm{A}(e_h, \psi - I_h\psi)$$
$$\le \| e_h \|_{\mathrm{A}} \| \psi - I_h\psi \|_{\mathrm{A}} .$$

If $e_h = 0$, the estimate is trivial. Otherwise, dividing by $\| e_h \|_{L^2(\Omega)}$ gives

$$\| e_h \|_{L^2(\Omega)} \le Ch\sqrt{1+A}\left(1 + C_P A\sqrt{2\alpha / e}\right) \| e_h \|_{\mathrm{A}} .$$

Combining this inequality with the energy-norm estimate yields

$$\| u - u_h \|_{L^2(\Omega)} \le Ch^2(1+A)\left(1 + C_P A\sqrt{2\alpha / e}\right)^2 \| f \|_{L^2(\Omega)} .$$

This completes the proof.

Thus, the conforming P_1 approximation retains first-order convergence in the $H^1(\Omega)$ -seminorm and second-order convergence in the $L^2(\Omega)$ -norm. The asymptotic convergence orders are independent of A and α , whereas the derived upper bounds on the error constants depend explicitly on the coefficient and regularity factors. In particular, the dependence on $\sqrt{\alpha}$ is consistent with the localization length $\ell_\alpha = \alpha^{-1/2}$. Consequently, maintaining a fixed level of accuracy as localization becomes sharper may require refinement of the mesh relative to ℓ_α. This mesh-localization interaction is investigated numerically in Section 5.

4.3 Discrete conditioning and localization effects

We next examine the conditioning of the finite element stiffness matrix. The parameter-robust bounds $1 \le a(z) \le 1 + A$ are sufficient for the continuous stability analysis. However, the lower bound $a(z) \ge 1$ is not sharp on the bounded computational domain. A more precise estimate is useful for identifying the effect of the localization parameter on the discrete system. Assume that $\Omega = (0,R)\times(0,Z)$ and $z_0 \in (0,Z)$. Define

$$d_\Omega := \max\{z_0, Z - z_0\}.$$

For $a(z) = 1 + A\exp\left[-\alpha(z - z_0)^2\right]$, the exact essential supremum and infimum of the coefficient on Ω are $a_{\max,\Omega} := \operatorname{ess\,sup}_{(r,z)\in\Omega} a(z) = 1 + A$ and $a_{\min,\Omega} := \operatorname{ess\,inf}_{(r,z)\in\Omega} a(z)$ $= 1 + A\exp(-\alpha d_\Omega^2)$. Consequently, the finite-domain coefficient contrast is

$$\rho_\Omega(A,\alpha) := \frac{a_{\max,\Omega}}{a_{\min,\Omega}} = \frac{1+A}{1+A\exp(-\alpha d_\Omega^2)}.$$

Unlike the uniform bound $1 + A$, the refined contrast factor explicitly contains both the amplitude A and the localization parameter α .

Proposition 4.2. Let K_h be the stiffness matrix associated with the conforming P_1 finite element method on a shape-regular and quasi-uniform triangulation. Then there exists $C > 0$, depending only on the domain and the mesh regularity constants but independent of h, A and α, such that

$$\kappa_2(K_h) \le Ch^{-2} \frac{1+A}{1+A\exp(-\alpha d_\Omega^2)}.$$

Proof. Let $K_h^{(0)}$ denote the stiffness matrix corresponding to the unit coefficient. For any coefficient vector X, let $v_h = \sum_{i=1}^{N_h} X_i \varphi_i$. Then

$$X^T K_h X = \int_\Omega a(z) \,|\nabla v_h|^2 \, dx,$$

whereas $X^T K_h^{(0)} X = \int_\Omega |\nabla v_h|^2 \, dx$. Therefore,

$$a_{\min,\Omega} X^T K_h^{(0)} X \le X^T K_h X \le a_{\max,\Omega} X^T K_h^{(0)} X.$$

Standard spectral estimates for conforming linear finite elements on shape-regular quasi-uniform meshes give [5], [13], [16] $\kappa_2\left(K_h^{(0)}\right) \le Ch^{-2}$. It follows that $\kappa_2(K_h) \le \frac{a_{\max,\Omega}}{a_{\min,\Omega}} \kappa_2\left(K_h^{(0)}\right)$,

and hence $\kappa_2(K_h) \le Ch^{-2} \frac{1+A}{1+A\exp(-\alpha d_\Omega^2)}$.

This completes the proof.

The refined factor

$$\rho_\Omega(A,\alpha) = \frac{1+A}{1+A\exp(-\alpha d_\Omega^2)}$$

clarifies the role of localization. For fixed $A > 0$, $\rho_\Omega(A,\alpha)$ is nondecreasing with respect to α. Moreover, $\lim_{\alpha\to 0} \rho_\Omega(A,\alpha) = 1$, whereas $\lim_{\alpha\to\infty} \rho_\Omega(A,\alpha) = 1 + A$. Thus, a broad Gaussian perturbation behaves increasingly like a nearly constant coefficient and has little effect on the matrix condition number apart from scaling. In contrast, stronger localization increases the effective coefficient contrast across the bounded domain. The global spectral estimate does not fully describe

whether the localized variation is adequately resolved by the mesh. For each element $K \in \mathrm{T}_h$, define $\mathrm{osc}_K(a) := \operatorname{ess\,sup}_K a - \operatorname{ess\,inf}_K a$. By the mean-value estimate, $\mathrm{osc}_K(a) \le h_K \| \nabla a \|_{L^\infty(K)}$. Using Proposition 3.3 gives $\mathrm{osc}_K(a) \le A\sqrt{2/e}\, h_K \sqrt{\alpha}$. Since $\eta_K = h_K \sqrt{\alpha}$, we obtain the mesh-dependent localization bound $\mathrm{osc}_K(a) \le A\sqrt{2/e}\, \eta_K$. This estimate identifies a second mechanism by which localization enters the discrete problem. The contrast factor $\rho_\Omega(A,\alpha)$ describes the global coefficient-contrast contribution to the spectral upper bound, whereas $\eta_K = h_K / \ell_\alpha$ measures the element size relative to the characteristic localization length. Neither estimate implies loss of coercivity, since $a(z) \ge 1$ for all admissible parameters. However, increasing α at fixed mesh resolution increases the derived upper bound on element-scale coefficient variation and may alter the spectrum of the assembled matrix. The theoretical bounds are upper estimates and do not determine the exact condition number. Their dependence on A, α and h will therefore be examined numerically in Section 5.

5 Numerical Experiments

Numerical experiments are performed to verify the theoretical results and to examine mesh-localization effects, stiffness-matrix conditioning, and solver performance.

5.1 Numerical setup and convergence verification

We first verify the theoretical convergence rates derived in Section 4.2. Consider the unit-square domain $\Omega = (0,1)\times(0,1)$ with homogeneous Dirichlet boundary conditions. For the convergence test, the Gaussian coefficient is chosen as

$$a(z) = 1 + 0.5\exp\left[-20(z-0.5)^2\right],$$

corresponding to $A = 0.5$, $\alpha = 20$, $z_0 = 0.5$.

A manufactured exact solution is prescribed as

$$u(r,z) = \sin(\pi r)\sin(\pi z).$$

The source term is then obtained from

$$f = -\nabla\cdot\left(a(z)\nabla u\right).$$

Since $a'(z) = -20(z-0.5)\exp\left[-20(z-0.5)^2\right]$,

the corresponding forcing function is

$$f(r,z) = 2\pi^2 a(z)\sin(\pi r)\sin(\pi z) + 20\pi(z-0.5)\exp\left[-20(z-0.5)^2\right]\sin(\pi r)\cos(\pi z).$$

This manufactured-solution construction permits the numerical errors to be evaluated directly. Uniform grids with $N = 20, 40, 80, 160$ subdivisions in each coordinate direction are considered. Let $\Delta_N := 1/N$ denote the nominal grid spacing. Since the triangulations are generated from the same structured-grid pattern, the finite element mesh size h is proportional to Δ_N. Thus, doubling N reduces both spatial scales by a factor of two. The errors are measured in the $H^1(\Omega)$ -seminorm and $L^2(\Omega)$ -norm. The experimental convergence rate is computed from

$$\text{Rate} = \frac{\log(E_N / E_{2N})}{\log 2}$$

where E_N denotes the corresponding error on the $N \times N$ grid [1], [3], [5].

Table 1. Convergence history of the finite element method for the manufactured solution with the localized Gaussian coefficient

Mesh	DOFs	H^1-seminorm error	Rate	L^2-norm error	Rate
20×20	361	1.7419e-01	—	3.5079e-03	—
40×40	1521	8.7201e-02	0.9983	8.7958e-04	1.9957
80×80	6241	4.3614e-02	0.9996	2.2006e-04	1.9989
160×160	25281	2.1808e-02	0.9999	5.5024e-05	1.9998

Source: created by the authors.

Table 1. shows a systematic reduction of both errors under mesh refinement. The observed -seminorm rates approach one, while the -norm rates approach two. These values agree with the theoretical estimates H^1 L^2 $\| u - u_h \|_V = O(h)$ and $\| u - u_h \|_{L^2(\Omega)} = O(h^2)$ derived in Section 4.2. For this fixed localized coefficient, the expected asymptotic convergence orders are retained. The dependence of the error magnitude on coefficient localization is examined separately in Section 5.2.

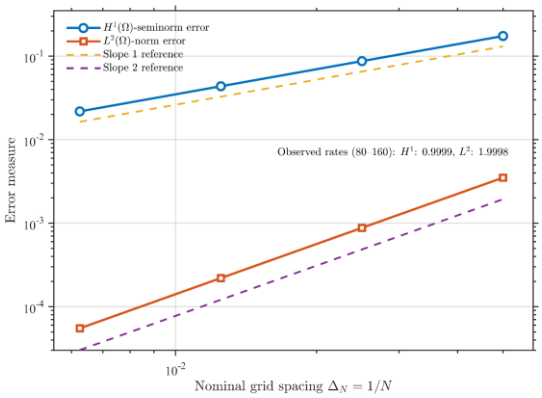

Fig. 1: Log-log convergence history of the finite element method for the manufactured solution. The -seminorm and -norm errors are plotted against the nominal grid spacing Reference slopes of one and two indicate the theoretical first- and second-order convergence rates, respectively P_1 $H^1(\Omega)$ $L^2(\Omega)$ $\Delta N = 1/N.$

Source: created by the authors.

Figure 1 compares the numerical error curves with the corresponding first- and second-order reference slopes. The nearly parallel behavior between the numerical error curves and the corresponding reference slopes confirms the expected asymptotic rates. The result provides a baseline verification of the finite element implementation before the stronger localization regimes are examined in Section 5.2

5.2 Mesh-localization interaction

We next examine the interaction between spatial resolution and the localization of the Gaussian coefficient. Section 3.5 introduced the characteristic localization length $\ell_\alpha = \alpha^{-1/2}$, while Section 4.3 established $\mathrm{osc}_K(a) \le A\sqrt{2/e}\, h_K \sqrt{\alpha}$. For fixed A, this motivates assessing mesh resolution through $h_K\sqrt{\alpha}$. This suggests that mesh resolution should be assessed relative to the localization scale rather than through the mesh size alone. The computations are performed on $\Omega = (0,1)\times(0,1)$ with $A = 4,\ z_0 = 0.5.$ Three representative localization parameters are considered: $\alpha \in \{2,10,40\}$. These values represent relatively broad, intermediate, and strongly localized Gaussian profiles, respectively. For each value of α, three uniform grid resolutions are used: $N = \{40,80,160\}$. Let $\Delta_N := 1/N$ denote the nominal grid spacing. Since the triangulations are generated from the same structured-grid pattern, Δ_N is proportional to the corresponding element diameter. We therefore introduce the dimensionless mesh-localization indicator $\eta_N := \Delta_N / \ell_\alpha = \Delta_N \sqrt{\alpha} = \sqrt{\alpha}/N.$ A smaller value of η_N corresponds to finer spatial resolution relative to the characteristic localization length. The same manufactured exact solution used in Section 5.1 is retained: $u(r,z) = \sin(\pi r)\sin(\pi z)$. For each value of α, the coefficient becomes

$$a(z) = 1 + 4\exp\left[-\alpha(z-0.5)^2\right].$$

The source term is recomputed from $f = -\nabla\cdot(a\nabla u)$, which gives

$$f(r,z) = 2\pi^2 a(z)\sin(\pi r)\sin(\pi z) + 8\pi\alpha(z-0.5)\exp\left[-\alpha(z-0.5)^2\right]\sin(\pi r)\cos(\pi z).$$

Thus, the exact solution is unchanged while the localization of the coefficient is varied. For every pair (N,α), define $E_{H^1} := \| \nabla(u-u_h) \|_{L^2(\Omega)}$ and $E_{L^2} := \| u-u_h \|_{L^2(\Omega)}$. The corresponding value of η_N is also recorded.

Table 2. Effect of mesh resolution and coefficient localization on the finite element error for and The dimensionless quantity measures the nominal grid spacing relative to the Gaussian localization scale

α	N	$\eta_N = \sqrt{\alpha}/N$	H^1 -seminorm error	L^2 -norm error
2	40	0.03536	8.7201e-02	8.5078e-04
2	80	0.01768	4.3614e-02	2.1285e-04
2	160	0.00884	2.1808e-02	5.3221e-05
10	40	0.07906	8.7208e-02	7.7956e-04
10	80	0.03953	4.3614e-02	1.9501e-04
10	160	0.01976	2.1809e-02	4.8759e-05
40	40	0.15811	8.7220e-02	7.0424e-04
40	80	0.07906	4.3616e-02	1.7614e-04
40	160	0.03953	2.1809e-02	4.4041e-05

Source: created by the authors.

For each fixed value of α, doubling N reduces η_N by a factor of two. Conversely, for a fixed grid resolution, increasing α increases η_N, indicating a coarser nominal resolution relative to the characteristic localization length. The numerical errors in Table 2 nevertheless retain the expected first-order H^1 -seminorm and second-order L^2 -norm convergence under mesh refinement for all three localization regimes. At a fixed mesh resolution, the H^1 -seminorm errors vary only slightly with α, whereas the L^2 -norm errors do not exhibit monotonic growth with increasing localization. Thus, η_N should be interpreted as a mesh-localization indicator rather than as a direct predictor of the finite element error magnitude. This interpretation is consistent with the local coefficient-oscillation estimate derived in Section 4.3,

$$\mathrm{osc}_K(a) \le A\sqrt{2/e}\, h_K \sqrt{\alpha}.$$

For fixed h_K, increasing α increases the derived upper bound on the coefficient variation within an element. Mesh refinement decreases this upper bound and improves the nominal resolution of the localized coefficient profile. However, the numerical results show that this geometric resolution indicator does not by itself determine the magnitude of the finite element error. To display the interaction more clearly, the two error measures are plotted against the dimensionless mesh-localization indicator. The resulting error trends are presented in Figure 2.

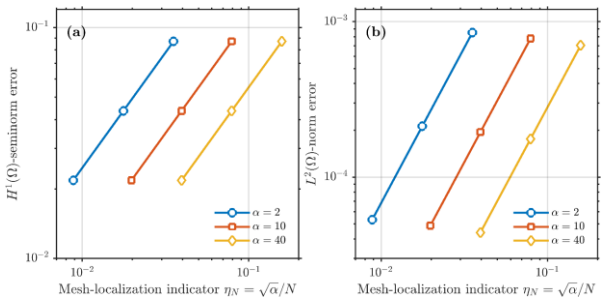

Fig. 2: Mesh-localization interaction for the Gaussian coefficient with and -seminorm error versus the dimensionless mesh-localization indicator -norm error versus Results are shown for and Smaller values of correspond to finer resolution relative to the Gaussian localization scale $A = 4$ $z_0 = 0.5$. (a). $H^1(\Omega)$ $\eta_N = \sqrt{\alpha}/N$. (b). $L^2(\Omega)$ η_N. $\alpha = 2{,}10{,}$ $40.$ η_N

Source: created by the authors.

The comparison of the three localization regimes provides a numerical assessment of the relationship between the mesh-localization indicator η_N and the finite element errors. No universal threshold for η_N is assumed. For each fixed value of α, decreasing η_N through mesh refinement produces a systematic reduction in both error measures while preserving the expected first-order H^1-seminorm and second-order L^2-norm convergence. At a fixed mesh resolution, however, the error magnitude is not determined solely by η_N: the H^1-seminorm errors vary only slightly with α, whereas the L^2-norm errors do not increase monotonically with localization. Thus, η_N is best interpreted as a geometric mesh-localization indicator rather than as a direct predictor of the finite element error. These results complement the parameter-dependent error analysis of Section 4.2 and motivate the conditioning study in Section 5.3.

5.3 Conditioning under amplitude and localization

We next examine how the amplitude and localization parameters affect the algebraic conditioning of the finite element system. Let $K_h U = F$ denote the discrete system introduced in Section 4.1. Since K_h is symmetric positive definite, its spectral condition number influences the convergence behavior of conjugate-gradient-type iterative solvers [13], [16]. The experiments are performed on $\Omega = (0,1)\times(0,1)$ using a uniform $N = 160$ grid and $z_0 = 0.5$. A numerical condition-number estimate is computed using $\hat{\kappa}_{1,h} := \mathrm{condest}(K_h)$. Here, $\hat{\kappa}_{1,h}$ denotes the estimated 1-norm condition number, whereas $\kappa_2(K_h)$ denotes the spectral condition number appearing in Proposition 4.2. Two parameter sweeps are considered. In the first experiment, $A \in \{0,1,2,4,8,16\}$, $\alpha = 10$. In the second experiment, $\alpha \in \{2,5,10,20,40\}$, $A = 4$. The same mesh, matrix assembly procedure, quadrature rule, and boundary treatment are used in both experiments. The common case $(A,\alpha) = (4,10)$ is obtained from the same assembled stiffness matrix in both parameter sweeps as an internal consistency check. For the present domain and $z_0 = 0.5$, $d_\Omega = 0.5$. Hence,

$$\rho_\Omega(A,\alpha) = \frac{1+A}{1+A\exp(-\alpha/4)}.$$

For fixed $\alpha > 0$, this factor increases with A, while for fixed $A > 0$ it increases with α. Moreover, $\lim_{\alpha\to 0}\rho_\Omega(A,\alpha) = 1$, $\lim_{\alpha\to\infty}\rho_\Omega(A,\alpha) = 1+A$. The theoretical estimate $\kappa_2(K_h) \le Ch^{-2}\rho_\Omega(A,\alpha)$ therefore provides an explicit parameter-dependent upper bound. Since the mesh is fixed in both sweeps, the factor h^{-2} is constant and the parameter dependence of this upper bound is contained in $\rho_\Omega(A,\alpha)$. Because $\mathrm{condest}(K_h)$ estimates a 1-norm condition number whereas Proposition 4.2 concerns $\kappa_2(K_h)$, the numerical experiment is not interpreted as a direct quantitative verification of the spectral bound. Instead, it is used to examine whether the same parameter-dependent trends are observed on the fixed mesh. The estimated condition numbers for the amplitude and localization sweeps are shown in Figure 3.

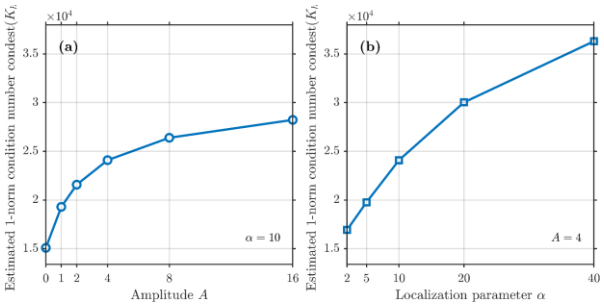

Fig. 3: Conditioning of the finite element stiffness matrix under Gaussian-coefficient parameter variation on a grid with Estimated 1-norm condition number versus amplitude for fixed Estimated 1-norm condition number versus localization parameter for fixed The common case is obtained from the same assembled stiffness matrix in both parameter sweeps 160×160 $z_0 = 0.5$. (a). condest(K_h) A $\alpha = 10$. (b). condest(K_h) α $A = 4$. $(A,\alpha) = (4,10)$

Source: created by the authors.

The numerical results show that the estimated 1-norm condition number increases systematically with both coefficient amplitude and localization. In the amplitude sweep with fixed $\alpha = 10$, condest(K_h) increases from 15087 at $A = 0$ to 28224 at $A = 16$. This trend is consistent with the increase of the finite-domain contrast factor $\rho_\Omega(A,\alpha)$. In the localization sweep with fixed $A = 4$, condest(K_h) increases from 16929 at $\alpha = 2$ to 36297 at $\alpha = 40$. This deterioration in discrete conditioning should not be interpreted as a loss of continuous coercivity, since $a(z) \geq 1$ for all admissible parameters. Rather, increasing localization affects both the finite-domain coefficient contrast and the spatial variation of the coefficient, as reflected in the estimates $\| \nabla a \|_{L^\infty(\Omega)} \leq A\sqrt{2\alpha / e}$ and $\mathrm{osc}_K(a) \leq A\sqrt{2/e}\, h_K \sqrt{\alpha}$. Thus, $\rho_\Omega(A,\alpha)$ characterizes the global finite-domain contrast contribution, whereas $h_K\sqrt{\alpha} = h_K / \ell_\alpha$ measures the element size relative to the localization length. In the localization sweep, both quantities vary with α, and the observed growth of condest(K_h) is consistent with the combined influence of coefficient contrast and localization on the assembled finite element system.

5.4 Solver robustness and computational performance

We finally examine the computational performance of the finite element implementation and the robustness of iterative solvers under coefficient variation. Since the stiffness matrix K_h is sparse, symmetric, and positive definite, the conjugate gradient method is applicable. To improve iterative convergence, an incomplete Cholesky factorization is used to construct the preconditioner [11], [13], [16] $M_h := L_h L_h^T$. where L_h denotes the incomplete Cholesky factor obtained from K_h. In the following comparisons, CG denotes the unpreconditioned conjugate gradient method, whereas IC-PCG denotes the conjugate gradient method with the incomplete Cholesky preconditioner. Let $r_k := F - K_h U_k$ denote the residual at iteration k. Both CG and IC-PCG are terminated when

$$\frac{\| r_k \|_2}{\| F \|_2} \leq 10^{-8}.$$

The same initial guess, stopping tolerance, maximum iteration limit, matrix assembly procedure, quadrature rule, and boundary treatment are used throughout the comparisons. The incomplete Cholesky settings are also held fixed in all IC-PCG tests. The zero vector is used as the initial guess, and the maximum iteration count is set to 5000. The incomplete Cholesky factorization is computed using the ICT option with drop tolerance 10^{-3} and diagonal compensation 10^{-3}; all reported timings are medians of five runs after an unreported warm-up run. For the solver tests, the right-hand side is generated from the same manufactured solution $u(r,z) = \sin(\pi r)\sin(\pi z)$ and is recomputed for each coefficient parameter set. This common computational protocol ensures that differences in solver behavior are associated with the coefficient parameters rather than with changes in the numerical implementation [13], [16]. Two computational experiments are performed. The first examines computational cost under mesh refinement. The coefficient parameters are fixed at $A = 4$, $\alpha = 10$, $z_0 = 0.5$ and the mesh resolutions are $N \in \{20, 40, 80, 160\}$. For an $N \times N$ structured grid with homogeneous Dirichlet boundary conditions, the number of unconstrained nodal degrees of freedom is $N_h = (N-1)^2$. For each mesh, the matrix assembly time and sparse-direct solution time are recorded. The reported total time is defined by

$$T_{\text{total}} := T_{\text{assembly}} + T_{\text{direct}}.$$

This experiment provides an empirical assessment of computational growth under mesh refinement. No asymptotic complexity is inferred beyond the range of meshes considered. Sparse direct solvers are used as a reference for the computational scaling of the discrete systems [14], [15]. The second experiment examines iterative solver robustness under representative coefficient variations. For the amplitude sweep, $A \in \{0, 4, 16\}$, $\alpha = 10$, whereas for the localization sweep, $\alpha \in \{2, 10, 40\}$, $A = 4$. In both sweeps, $z_0 = 0.5$,

$N = 160$. The values represent low, intermediate, and relatively strong parameter regimes while keeping the computational comparison compact. The common case $(A, \alpha) = (4, 10)$ is assembled only once. The same stiffness matrix and right-hand side are used for this case in both parameter sweeps. This provides an internal consistency check for the numerical implementation. For IC-PCG, the reported solver time includes both the incomplete Cholesky setup and the subsequent iterative solution,

$$T_{\text{IC-PCG}} := T_{\text{IC setup}} + T_{\text{PCG}}.$$

This convention permits a fairer comparison with the unpreconditioned CG solver by accounting for the computational cost of constructing the preconditioner.

Table 3. Computational scaling and iterative solver robustness for the localized Gaussian coefficient model. (a) Mesh-refinement timing results for fixed and (b) CG and incomplete-Cholesky-preconditioned CG performance under representative amplitude and localization parameters on an grid with relative residual tolerance The reported IC-PCG time includes both preconditioner construction and iterative solution

(a) Mesh-refinement performance

N	DOFs	Assembly time (s)	Direct solve time (s)	Total time (s)
20	361	0.001132	0.000265	0.001397
40	1,521	0.002363	0.001525	0.003888
80	6,241	0.004737	0.005661	0.010398
160	25,281	0.021847	0.026972	0.048819

(b) Iterative solver performance

Sweep parameter	Value	CG iter.	CG time (s)	IC-PCG iter.	IC-PCG time (s)
A	0	202	0.040807	26	0.049471
A	4	371	0.067406	32	0.055069
A	16	423	0.081486	34	0.059246
α	2	262	0.050113	30	0.051242
α	10	371	0.067406	32	0.055069
α	40	505	0.094350	29	0.049899

Table 3. summarizes the mesh-refinement timings and the performance of CG and IC-PCG. Panel (a) shows the computational growth associated with mesh refinement. As increases from 20 to 160, the number of unconstrained degrees of freedom increases from 361 to 25,281. Correspondingly, both matrix assembly and sparse-direct solution times increase, with the total measured time rising from 0.001397 s to 0.048819 s. These timings provide an empirical description of the computational cost over the tested mesh range and are not used to infer an asymptotic complexity. Panel (b) demonstrates the sensitivity of unpreconditioned CG to coefficient amplitude and localization. In the amplitude sweep, the CG iteration count increases from 202 at to 423 at while in the localization sweep it increases from 262 at to 505 at In contrast, the IC-PCG iteration counts remain within the narrow range 26–34 over all tested cases. This substantially reduced variation indicates that incomplete Cholesky preconditioning improves the robustness of the iterative solution with respect to both amplitude and localization. The timing results also show that the additional preconditioner setup cost may not be advantageous for the easiest cases, but becomes beneficial as the unpreconditioned system becomes more difficult [11], [13], [16]. The amplitude sweep is interpreted together with the finite-domain contrast factor derived in Section 4.3, $N\ A = 0\ A = 16$, $\alpha = 2$ $\alpha = 40$.

$$\rho_{\Omega}(A, \alpha) = \frac{1 + A}{1 + A\exp(-\alpha / 4)}.$$

For fixed $\alpha = 10$, increasing A increases the finite-domain coefficient contrast and is accompanied by increases in both the estimated stiffness-matrix condition number and the unpreconditioned CG iteration count. For the localization sweep, the contrast factor also depends explicitly on α. Localization further influences the spatial variation of the coefficient through $\| \nabla a \|_{L^{\infty}(\Omega)} \le A\sqrt{2\alpha / e}$ and, at the element level, $\text{osc}_K(a) \le A\sqrt{2/e}\, h_K \sqrt{\alpha}$. Since the mesh is fixed in the localization sweep, increasing α also increases the dimensionless mesh-localization quantity $h_K \sqrt{\alpha} = h_K / \ell_{\alpha}$. Thus, the localization experiment reflects the combined effects of finite-domain coefficient contrast and coefficient variation relative to the mesh scale. The numerical results show that the unpreconditioned CG iteration count increases substantially with both amplitude and localization, whereas the IC-PCG iteration counts remain within the narrow range 26–34 over all tested cases. This reduced variation indicates that incomplete Cholesky preconditioning improves the robustness of the iterative solution over the parameter regimes considered. No claim of parameter-independent convergence is made beyond the numerical regimes examined here.

6 Discussion

The results clarify the distinct roles of coefficient amplitude and localization in the variable-coefficient elliptic problem. The continuous problem remains uniformly coercive because $a(z) \ge 1$ for all admissible values of A and α. Hence, increasing either

parameter does not reduce the lower ellipticity bound. The amplitude A enters the continuity bound through the upper coefficient bound $1+A$. In contrast, the localization parameter α does not affect the parameter-robust lower ellipticity bound, but it strongly influences the spatial variation of the coefficient. This distinction is reflected in the parameter-explicit regularity estimate developed in Section 3.6.

The finite element results are consistent with the theoretical approximation analysis. The conforming P_1 method retains first-order convergence in the $H^1(\Omega)$ -seminorm and second-order convergence in the $L^2(\Omega)$ -norm. These orders are preserved despite the localized Gaussian coefficient. This agrees with standard finite element theory for sufficiently regular elliptic problems [1], [3], [5]. The parameters mainly influence the constants in the derived error bounds rather than the asymptotic convergence orders.

The mesh-localization study provides a more detailed interpretation of the role of α. The quantity $\eta_N = \sqrt{\alpha}/N$ measures the nominal mesh spacing relative to the localization length. Smaller values of η_N correspond to finer relative resolution. However, the numerical results show that η_N is not a direct predictor of the finite element error magnitude. At fixed N, the H^1 -seminorm error changes only slightly with α, while the L^2 -norm error does not increase monotonically. Thus, η_N is better interpreted as a geometric resolution indicator. Its importance lies in describing how the mesh resolves the localized coefficient rather than in prescribing a universal error threshold.

A stronger localization effect is observed in the algebraic conditioning. The estimated 1-norm condition number increases with both A and α on the fixed mesh. This behavior is consistent with the finite-domain coefficient contrast of Section 4.3 and the coefficient-variation estimates derived in Sections 3.5 and 4.3. Importantly, this deterioration is a discrete effect. It should not be interpreted as a loss of continuous coercivity. The continuous lower ellipticity bound remains unchanged even when the assembled stiffness matrix becomes more difficult to solve.

The iterative solver results support this interpretation. The unpreconditioned CG iteration count increases from 202 to 423 over the amplitude sweep and from 262 to 505 over the localization sweep. In contrast, IC-PCG requires only 26–34 iterations over all tested cases. The incomplete Cholesky preconditioner therefore reduces the sensitivity of iterative convergence to coefficient variation. Its setup cost can make it less attractive for the easiest systems. For several of the more difficult tested cases, however, the reduced iteration count also leads to lower computational time. This behavior is consistent with the expected role of preconditioning for symmetric positive definite systems [11], [13], [16].

The conclusions should be interpreted within the scope of the present model. The study uses an unweighted two-dimensional meridional formulation, a Gaussian coefficient depending only on z, and a rectangular domain. The numerical verification also uses a manufactured solution and a finite range of parameter values. Moreover, the MATLAB function condest provides an estimated 1-norm condition number, whereas the theoretical bound in Proposition 4.2 concerns the spectral condition number. The numerical conditioning study should therefore be viewed as supporting the predicted parameter-dependent trends rather than as a direct quantitative verification of that spectral bound. Extensions to more general coefficient distributions, nonrectangular domains, adaptive meshes, and fully axisymmetric formulations would provide useful directions for further investigation.

7 Conclusion

This study investigated a variable-coefficient elliptic problem with a localized Gaussian coefficient. The analysis separated the effects of coefficient amplitude and localization. The problem remains uniformly coercive for all admissible parameters because the coefficient satisfies $a(z) \geq 1$. At the same time, stronger localization increases the derived upper bound on the spatial variation of the coefficient. This effect enters the higher-order regularity and finite element error bounds.

A conforming P_1 finite element approximation was analyzed with explicit parameter dependence. The numerical results confirmed first-order convergence in the $H^1(\Omega)$ -seminorm and second-order convergence in the $L^2(\Omega)$ -norm. These convergence orders were preserved over the tested localization regimes. The mesh-localization indicator $\eta_N = \sqrt{\alpha}/N$ provided a useful measure of relative spatial resolution. However, it did not directly determine the finite element error magnitude.

The discrete conditioning results showed a stronger dependence on the coefficient parameters. The estimated 1-norm condition number increased

with both amplitude and localization on the fixed mesh. This deterioration did not indicate a loss of continuous coercivity. Instead, it reflected changes in coefficient contrast and spatial variation at the discrete level.

The solver experiments further showed that unpreconditioned CG became more sensitive as the amplitude or localization parameter increased. In contrast, IC-PCG maintained a much narrower range of iteration counts over the tested cases. These results support the practical value of incomplete Cholesky preconditioning over the parameter regimes considered here. Future work may extend the present framework to adaptive meshes, more general coefficient distributions, nonrectangular domains, and fully axisymmetric formulations.

Acknowledgement:
The authors would like to thank the Department of Mathematics, Faculty of Science, Srinakharinwirot University, for academic support.

Declaration of Generative AI and AI-assisted Technologies in the Writing Process

During the preparation of this work, the author(s) utilized artificial intelligence (AI) technologies solely for the purpose of linguistic refinement and grammatical correction. Following the application of these tools, the author(s) comprehensively reviewed, verified, and edited the resulting text. The author(s) maintain full accountability and responsibility for the accuracy, integrity, and final content of the publication.

References:

[1] Z. Chen, Finite Element Methods and Their Applications, Springer, Berlin, 2005; ISBN: 978-3-540-24078-5; doi: 10.1007/3-540-28078-2.

[2] P. Knabner and L. Angermann, Numerical Methods for Elliptic and Parabolic Partial Differential Equations, Springer, New York, 2003; ISBN: 978-0-387-95449-3; doi: 10.1007/b97419.

[3] P. G. Ciarlet, The Finite Element Method for Elliptic Problems, North-Holland, Amsterdam, 1978; ISBN: 978-0-444-85028-7.

[4] I. Babuška, Error bounds for finite element method, Numer. Math., Vol. 16, 1971, pp. 322–333; doi: 10.1007/BF02165003.

[5] A. Ern and J. L. Guermond, Theory and Practice of Finite Elements, Springer, New York, 2004; ISBN: 978-0-387-20574-8; doi: 10.1007/978-1-4757-4355-5.

[6] S. C. Brenner, C. Cavanaugh and L.-Y. Sung, A Hodge decomposition finite element method for an elliptic Maxwell boundary value problem on general polyhedral domains, Comput. Methods Appl. Math., Vol. 25, No. 4, 2025, pp. 823–848; doi: 10.1515/cmam-2025-0100.

[7] W. Yang, X. Liu, B. He and Y. Q. Huang, A posteriori error estimator of SDG method for variable-coefficients time-harmonic Maxwell's equations, J. Comput. Math., Vol. 41, 2023, pp. 263–286; doi: 10.4208/jcm.2112-m2020-0330.

[8] L. Li, M. Lyu and W. Zheng, An energy-stable finite element method for nonlinear Maxwell's equations, J. Comput. Phys., Vol. 486, 2023, Article ID 112135; doi: 10.1016/j.jcp.2023.112135.

[9] T. Chaumont-Frelet, S. Lanteri and P. Vega, A posteriori error estimates for finite element discretizations of time-harmonic Maxwell's equations coupled with a non-local hydrodynamic Drude model, Comput. Methods Appl. Mech. Eng., Vol. 385, 2021, Article ID 114002; doi: 10.1016/j.cma.2021.114002.

[10] T. Chaumont-Frelet and P. Vega, Frequency-explicit a posteriori error estimates for finite element discretizations of Maxwell's equations, SIAM J. Numer. Anal., Vol. 60, 2022, pp. 1774–1798; doi: 10.1137/21M1421805.

[11] M. Benzi, Preconditioning techniques for large linear systems: a survey, J. Comput. Phys., Vol. 182, 2002, pp. 418–477; doi: 10.1006/jcph.2002.7176.

[12] J. Xu and L. Zikatanov, Algebraic multigrid methods, Acta Numer., Vol. 26, 2017, pp. 591–721; doi: 10.1017/S0962492917000083.

[13] H. Elman, D. Silvester and A. Wathen, Finite Elements and Fast Iterative Solvers: with Applications in Incompressible Fluid Dynamics, 2nd ed., Oxford University Press, Oxford, 2014; ISBN: 978-0-19-967879-2; doi: 10.1093/acprof:oso/9780199678792.001.0001.

[14] P. R. Amestoy, I. S. Duff, J. Y. L'Excellent and J. Koster, A fully asynchronous multifrontal solver using distributed dynamic scheduling, SIAM J. Matrix Anal. Appl., Vol. 23, 2001, pp. 15–41; doi: 10.1137/S0895479899358194.

[15] T. A. Davis, Algorithm 1000: SuiteSparse:GraphBLAS: Graph Algorithms in the Language of Sparse Linear Algebra, ACM Trans. Math. Softw., Vol. 45, No. 4, 2019, Article 44, pp. 1–25; doi: 10.1145/3322125.

[16] Y. Saad, Iterative Methods for Sparse Linear Systems, 2nd ed., SIAM, Philadelphia, 2003; ISBN: 978-0-89871-534-7; doi: 10.1137/1.9780898718003.

[17] E. A. Spence, Preconditioning FEM discretisations of the high-frequency Helmholtz and Maxwell equations by either perturbing the coefficients or adding absorption, Comput. Math. Appl., Vol. 210, 2026, pp. 186–199; doi: 10.1016/j.camwa.2026.03.009.

[18] L. Li, Y. He and X. Feng, A difference virtual element method for the 3D elliptic equation with the variable coefficient on general cylindrical domains, Int. J. Numer. Anal. Model., Vol. 22, 2025, pp. 96–112; doi: 10.4208/ijnam2025-1005.

Contribution of Individual Authors to the Creation of a Scientific Article (Ghostwriting Policy)

The authors equally contributed to the present research, at all stages from the formulation of the problem to the final findings and solution.

Sources of Funding for Research Presented in a Scientific Article or Scientific Article Itself

No funding was received for conducting this study.

Conflict of Interest

The authors have no conflicts of interest to declare.

Creative Commons Attribution License 4.0 (Attribution 4.0 International, CC BY 4.0)

This article is published under the terms of the Creative Commons Attribution License 4.0 https://creativecommons.org/licenses/by/4.0/deed.en_US